

NONTHERMAL PARTICLE ACCELERATION IN 3D RELATIVISTIC MAGNETIC RECONNECTION IN PAIR PLASMA

GREGORY R. WERNER¹ AND DMITRI A. UZDENSKY^{1,2}

¹*Center for Integrated Plasma Studies, Physics Department,
390 UCB, University of Colorado, Boulder, CO 80309, USA*

²*Institute for Advanced Study, 1 Einstein Dr., Princeton, NJ 08540, USA*

ABSTRACT

As a fundamental process converting magnetic to plasma energy in high-energy astrophysical plasmas, relativistic magnetic reconnection is a leading explanation for the acceleration of particles to the ultrarelativistic energies necessary to power nonthermal emission (especially X-rays and gamma-rays) in pulsar magnetospheres and pulsar wind nebulae, corone and jets of accreting black holes, and gamma-ray bursts. An important objective of plasma astrophysics is therefore the characterization of nonthermal particle acceleration (NTPA) effected by reconnection. Reconnection-powered NTPA has been demonstrated over a wide range of physical conditions using large two-dimensional (2D) kinetic simulations. However, its robustness in realistic 3D reconnection—in particular, whether the 3D relativistic drift-kink instability (RDKI) disrupts NTPA—has not been systematically investigated, although pioneering 3D simulations have observed NTPA in isolated cases. Here we present the first comprehensive study of NTPA in 3D relativistic reconnection in collisionless electron-positron plasmas, characterizing NTPA as the strength of 3D effects is varied systematically via the length in the third dimension and the strength of the guide magnetic field. We find that, while the RDKI prominently perturbs 3D reconnecting current sheets, it does not suppress particle acceleration, even for zero guide field; fully 3D reconnection robustly and efficiently produces nonthermal power-law particle spectra closely resembling those obtained in 2D. This finding provides strong support for reconnection as the key mechanism powering high-energy flares in various astrophysical systems. We also show that strong guide fields significantly inhibit NTPA, slowing reconnection and limiting the energy available for plasma energization, yielding steeper and shorter power-law spectra.

Keywords: acceleration of particles — magnetic reconnection — relativistic processes
— pulsars: general — gamma-ray burst: general — galaxies: jets

1. INTRODUCTION

A long-standing puzzle in high-energy plasma astrophysics is the mechanism behind nonthermal particle acceleration (NTPA) that produces power-law X-ray and γ -ray spectra observed in pulsar wind nebulae (PWN), coronae and jets of accreting black holes (BHs) in X-ray Binaries (XRBs) and Active Galactic Nuclei (AGN) including blazars, and Gamma Ray Bursts (GRBs). A leading candidate is magnetic reconnection, a basic plasma process that rapidly converts magnetic into particle kinetic energy through magnetic field rearrangement and relaxation. In the high-energy universe, magnetic reconnection is often relativistic: the energy density of the reconnecting magnetic field B_0 exceeds that of the ambient plasma (including rest-mass), heating plasma to relativistic temperatures, driving relativistic flows, and accelerating particles to ultrarelativistic energies. Relativistic reconnection has been invoked in electron-ion or mixed-composition plasmas in accreting BH coronae (Beloborodov 2017), GRBs (Drenkhahn & Spruit 2002; Giannios 2008; McKinney & Uzdensky 2012), and blazar jets (Giannios et al. 2009; Nalewajko et al. 2011), but also, especially, in electron-positron pair plasmas in pulsar magnetospheres (Lyubarsky 1996; Uzdensky & Spitkovsky 2014; Cerutti et al. 2015), pulsar winds (Coroniti 1990; Arka & Dubus 2013), PWN (Uzdensky et al. 2011; Cerutti et al. 2012a, 2013, 2014a), and magnetar flares (Lyutikov 2003, 2006; Uzdensky 2011). Beyond its astrophysical applications, relativistic pair reconnection is important as the simplest reconnection scenario, a reference case for studying effects of plasma composition, collisions, radiation, etc.

Recently, first-principles particle-in-cell (PIC) kinetic simulations have significantly advanced understanding of NTPA in relativistic pair-plasma reconnection, mostly in two dimensions (2D) (Zenitani & Hoshino 2001, 2005, 2007; Jaroschek et al. 2004; Lyubarsky & Liverts 2008; Liu et al. 2011; Bessho & Bhattacharjee 2007; Cerutti et al. 2012b, 2013; Sironi & Spitkovsky 2014; Guo et al. 2014, 2015; Liu et al. 2015; Sironi et al. 2015, 2016; Werner et al. 2016), with a few three-dimensional (3D) studies (Jaroschek et al. 2004; Zenitani & Hoshino 2008; Cerutti et al. 2014b; Kagan et al. 2013; Sironi & Spitkovsky 2014; Guo et al. 2014, 2015). Such studies are very challenging because even the qualitative character of reconnection dynamics, hence also NTPA, depends on the scale separation between the global system size L and the microscopic plasma scales, e.g., the average electron gyroradius in the reconnection layer, $\bar{\rho}_e = \bar{\gamma}m_e c^2 / eB_0$, where $\bar{\gamma}m_e c^2$ is the average relativistic energy of electrons energized by reconnection. When $L/\bar{\rho}_e$ is large, as in astrophysical systems, reconnection is highly dynamic, with many secondary magnetic islands (plasmoids, or in 3D, flux ropes) and inter-plasmoid current sheets (Bhattacharjee et al. 2009; Uzdensky et al. 2010; Loureiro et al. 2012). The relevant large-system plasmoid-dominated regime, in which reconnection characteristics like the particle energy distribution $f(\gamma)$ no longer depend on L , is realized above a critical size $L_c \sim 10^2 \bar{\rho}_e$ (Werner et al. 2016).

Only recently have 2D PIC simulations managed to probe this large-system regime systematically, confirming reconnection-powered NTPA (e.g., Sironi & Spitkovsky 2014; Guo et al. 2014, 2015; Sironi et al. 2015; Werner et al. 2016). Importantly, they mapped out key acceleration parameters versus L and the ambient plasma and magnetic field conditions, which are characterized by “cold” and “hot” plasma magnetizations, $\sigma \equiv B_0^2 / 4\pi n_b m_e c^2$ and $\sigma_h \equiv B_0^2 / 4\pi h$ (see, e.g., Melzani et al. 2014), where B_0 is the reconnecting magnetic field, n_b is the upstream (background) particle density, and h is the upstream relativistic plasma enthalpy density including the rest-mass contribution $n_b m_e c^2$. Thus the particle energy power-law index, $p(L, \sigma_h) \equiv -d \ln f / d \ln \gamma$, was found to become independent of L as $L \rightarrow \infty$, approaching a value consistent with 1 in the ultrarelativistic limit $\sigma_h \simeq \sigma \gg 1$ (in 2D

simulations with no guide field, Guo et al. 2014; Werner et al. 2016). In addition, Werner et al. (2016) investigated the high-energy cutoff $\gamma_c(L, \sigma)$ of $f(\gamma)$: for large systems, $\gamma_c \sim 4\sigma$ (independent of L), while for small systems, $\gamma_c \sim 0.1L/\rho_0$, where $\rho_0 \equiv m_e c^2/eB_0$. These empirical results thus identified the above-mentioned critical size $L_c \simeq 40\sigma\rho_0$, where the two cutoffs meet, beyond which the NTPA properties become insensitive to L .

However, these large-scale 2D studies naturally cannot describe the fundamentally-3D nature of reconnection dynamics, including the rapid development of the relativistic drift-kink instability (RDKI), whose effect on NTPA is still debated. Whereas Zenitani & Hoshino (2008) claimed that RDKI suppresses particle acceleration in 3D, recent studies (Sironi & Spitkovsky 2014; Guo et al. 2014) suggest that RDKI eventually saturates, restoring (2D-like) NTPA. If RDKI suppresses NTPA, a guide magnetic field (which suppresses RDKI) may bolster particle acceleration (Zenitani & Hoshino 2008); this issue, however, remains unsettled.

Resolving these important issues requires a thorough, systematic study characterizing 3D effects on NTPA using large simulations. To accomplish this, we perform a set of 3D PIC simulations with varying box aspect ratio L_z/L_x and guide magnetic field B_{gz} , which govern the three-dimensionality of the reconnection process (e.g., small L_z or large B_{gz} suppress RDKI). Focusing on particle energy spectra, we then present an unambiguous demonstration of NTPA in relativistic pair-plasma reconnection, comprehensively characterizing NTPA from 2D to 3D. Specifically, we describe the power-law index p as a function of L_z/L_x and B_{gz} , showing that: (1) despite RDKI, 3D reconnection drives NTPA as efficiently as 2D reconnection, yielding remarkably similar spectra; (2) modest guide fields $B_{gz} \lesssim B_0/4$ barely affect NTPA, but strong $B_{gz} \gtrsim B_0$ dramatically suppress NTPA, yielding steeper spectra. Our results can provide useful prescriptions for particle spectra produced by reconnection for comparison with astrophysical observations.

2. SIMULATIONS

Using the electromagnetic PIC code Zeltron (Cerutti et al. 2013), we run simulations in a box of size $L_x \times L_y \times L_z$ with periodic boundary conditions; here, x is the direction of reconnecting magnetic field, y is perpendicular to the current layers, and the third dimension z parallels the initial current and guide field. The 3D set-up extends the 2D double-periodic systems used in our previous paper (Werner et al. 2017) uniformly in z .

The initial state is described by the reversing magnetic field B_x and background ultrarelativistic Maxwell-Jüttner pair plasma with temperature $\theta_b = kT_b/m_e c^2 = 275$ and combined electron and positron density n_b . Conforming to periodic boundary conditions, the magnetic field undergoes two reversals (supported by two initial current layers of half-thickness δ), $B_x(y) = \pm B_0 \tanh[(y - y_{1,2})/\delta]$, where $y_1 = L_y/4$ and $y_2 = 3L_y/4$ are the midplanes of the two layers. A uniform guide field B_{gz} is added in the z -direction; we explore $B_{gz}/B_0 \in \{0, 0.25, 0.5, 1, 2\}$.

To study magnetically-dominated reconnection, we initialize the upstream plasma with the largest “hot” magnetization resolving the Debye length (described below), $\sigma_h \equiv B_0^2/(4\pi h) = 25$ (where $h = 4n_b\theta_b m_e c^2$ in the relativistic limit, cf. Melzani et al. 2014). The “cold” magnetization, which sets the overall simulation scale and could be anything consistent with $\sigma_h = 25$ and $\theta_b \gg 1$, is $\sigma \equiv B_0^2/(4\pi n_b m_e c^2) = 4\theta_b\sigma_h = 2.75 \times 10^4$, as in Werner et al. (2017).

The two current layers are relativistic Harris sheets (Kirk & Skjæraasen 2003) with simulation-frame density $n_d(y) = n_{d0} \cosh^{-2}[(y - y_{1,2})/\delta]$. Within each sheet, electrons and positrons drift with opposite average velocities $\pm\beta_{\text{drift}}c\hat{z}$ to generate the current supporting the magnetic field reversal,

i.e., satisfying Ampere's Law with $\delta = B_0/(4\pi en_{d0}\beta_{\text{drift}})$. The Harris sheets also provide pressure balance, with rest-frame temperature $\theta_d = (1/2)\gamma_{\text{drift}}(n_b/n_{d0})\sigma = 50\gamma_{\text{drift}}(n_b/n_{d0})\theta_b$, where $\gamma_{\text{drift}} = (1 - \beta_{\text{drift}}^2)^{-1/2}$. Here we use $\theta_b = 275$, $n_{d0}/n_b = 5$, and $\beta_{\text{drift}} = 0.3$, hence $\gamma_{\text{drift}} \simeq 1.05$, and $\theta_d = 2890$.

In nonradiative ultrarelativistic pair reconnection, lengths and times scale with σ ; as long as $\theta_b \gg 1$, simulations with the same σ_h but different σ are equivalent after rescaling. Thus, we define a characteristic length scale $\rho_c \equiv 2\sigma\rho_0 = 2\sigma m_e c^2/eB_0$, 4 times the gyroradius of a particle with energy $B_0^2/(8\pi n_b)$.¹ The corresponding timescale is $\omega_c \equiv c/\rho_c$. Convergence studies led us to choose 40 total macroparticles per cell and grid cell size $\Delta x = \Delta y = \Delta z = \rho_c/24$, sufficient to resolve both the evolved and initial ($\delta = 8\Delta x = \rho_c/3$) current-layer thicknesses, and also the upstream Debye length ($\lambda_D = 1.2\Delta x$), preventing unphysical finite-grid heating (Langdon 1970). We use the Courant-Friedrichs-Lewy timestep $\Delta t = 0.99\Delta x/(\sqrt{3}c)$ and typically run until $t \approx 5L_x/c$ (i.e., $t \approx 200/\omega_c$ for $L_x = 40\rho_c$). These parameters yielded better than 1% energy conservation.

We show results mostly for the fiducial size $L_x = 40\rho_c = 80\sigma\rho_0$, with additional $L_x = 20\rho_c$ and $L_x = 64\rho_c$ simulations for $B_{gz} = 0$. All systems have $L_y = 2L_x$ to prevent undesirable interaction between the two layers. By varying L_z from a single cell (2D) up to $4L_x$, we explore the 3D nature of reconnection.

As in many 2D reconnection studies, the initial magnetic field is perturbed uniformly in z , as described by the vector potential, e.g., for the lower layer

$$A_z = \left[1 + 0.01 \cos \frac{2\pi x}{L_x} \cos^2 \frac{2\pi(y - y_1)}{L_y} \right] B_0 \delta \left[\ln \cosh \frac{y_2 - y_1}{2\delta} - \ln \cosh \frac{y - y_1}{\delta} \right]. \quad (1)$$

In all our 2D simulations, and in 3D simulations with $B_{gz} \geq 0.25B_0$, the presence of a perturbation does not change the reconnection rate or NTPA. In perturbationless 3D runs with $B_{gz} = 0$, however, particles from the dense initial Harris sheet avoid becoming trapped in flux ropes, and instead spread about the layer, increasing the immediately-upstream density, effectively lowering σ_h , and significantly slowing reconnection and hindering NTPA. Leaving details for a future publication, we emphasize that initializing 3D $B_{gz} = 0$ simulations with a perturbation makes them more closely resemble (2D and 3D) $B_{gz} = B_0/4$ simulations.

3. RESULTS

Our main findings are: (1) magnetic energy dissipation and nonthermal particle acceleration (NTPA) are largely unaffected by three-dimensionality, i.e., by L_z/L_x ; and (2) a strong guide field reduces the rate and amount of magnetic dissipation and inhibits NTPA.

We illustrate these results with plots showing energy dissipation and final particle energy spectra in simulations with $L_x = 40\rho_c = 80\sigma\rho_0$, for L_z/L_x ranging from 0.001 (one cell in z) up to 1 (and up to $L_z/L_x = 2$ for $B_{gz} = B_0$ and 4 for $B_{gz} = 0$), and for $B_{gz}/B_0 \in \{0, 0.25, 0.5, 1, 2\}$, all with $\sigma_h = 25$.

In agreement with previous 3D studies (Zenitani & Hoshino 2008; Kagan et al. 2013; Cerutti et al. 2014b), we find that reconnection proceeds through rapid growth of tearing (plasmoid) and RDKI instabilities, quickly disrupting the initial current sheet and generating a complex, dynamic hierarchy of interacting flux ropes. Although RDKI has clearly-visible effects (e.g., current-layer kinking in the yz plane, Fig. 1, left), magnetic dissipation is similar in 2D and 3D. Figure 1 (right) shows the evolution of transverse magnetic energy, $U_{\text{mag},xy} \equiv \int (B_x^2 + B_y^2)/8\pi dV$, for different values of B_{gz}

¹ This definition agrees with Werner et al. (2017), but differs from $\rho_c \equiv \theta_d\rho_0$ used by Werner et al. (2016).

and L_z/L_x . This evolution is typical for a closed system: reconnection ramps up gradually and continues until the available free magnetic energy is exhausted. The released $U_{\text{mag},xy}$ is converted mostly into particle kinetic energy, with some into $U_{\text{mag},z} \equiv \int B_z^2/8\pi dV$ and a small amount into the electric field (Table 1).

Overall, energy dissipation differs little between 2D and $L_z/L_x \gtrsim 1$; however, 3D simulations with weak guide field ($B_{gz} \lesssim B_0/4$) dissipate slightly more energy than their 2D counterparts by accessing final relaxed states that are nonuniform in z , e.g., slightly kinked flux ropes with lower magnetic energy than the straight (translationally-symmetric in z) flux ropes that are the only possibility in 2D. In 2D or nearly 2D runs with $B_{gz} = 0$, $U_{\text{mag},xy}$ fell by $\sim 40\%$ from initial to final state, while decreasing by 46% for $L_z/L_x = 2$ (Fig. 1, right). A modest $B_{gz} \gtrsim 0.5$, however, stabilizes the kink (for the explored range of $L_z/L_x \leq 2$), resulting in nearly identical 2D and 3D energy budgets.

While L_z/L_x has little effect, we find that B_{gz} significantly influences all aspects of reconnection. As expected, a strong guide field ($B_{gz} \gtrsim B_0$) suppresses RDKI (Zenitani & Hoshino 2007, 2008). In addition, it slows down reconnection and reduces the total dissipated magnetic energy, equally in 2D and 3D. We attribute these effects to the guide field's effective inertia and pressure, respectively (see also Dahlin et al. 2016); since the guide field is approximately frozen into the plasma, its magnetic enthalpy $h_{\text{mag},z} \equiv B_{gz}^2/4\pi$ lowers the effective σ_h -parameter,

$$\sigma_{h,\text{eff}} \equiv B_0^2/4\pi(h + h_{\text{mag},z}) = B_0^2/(4\pi h + B_{gz}^2), \quad (2)$$

which governs the relevant transverse Alfvén speed, $V_A = c\sigma_{h,\text{eff}}^{1/2}/(1 + \sigma_{h,\text{eff}})^{1/2} = cB_0/(4\pi h + B_0^2 + B_{gz}^2)^{1/2}$. In the high- σ_h regime, $B_0^2 \gg 4\pi h$, V_A falls to $V_A/c \approx B_0/(B_0^2 + B_{gz}^2)^{1/2}$, becoming subrelativistic for strong guide field ($B_{gz} \gg B_0$), thereby reducing the reconnection rate, $E_{\text{rec}} \sim 0.1B_0V_A/c$, to $\sim 0.1B_0^2/B_{gz}$.

In addition, since a strong B_{gz} makes the plasma less compressible, it also affects the final relaxed state (Uzdensky et al. 1996). In particular, the tension force of reconnected field lines that contracts plasmoids must perform work against the combined plasma and guide-field pressure; a strong B_{gz} resists compression and makes the plasmoids stiffer, reducing the work that can be done and hence the overall amount of $U_{\text{mag},xy}$ released by reconnection. Moreover, since some of the released $U_{\text{mag},xy}$ is spent compressing B_z , the fraction of the energy that goes to particles is also reduced (Table 1).

Most of the released $U_{\text{mag},xy}$ goes to particles, producing a nonthermal power-law spectrum in both 2D and 3D. We will show particle energy spectra $f(\gamma) = dN/d\gamma$ at late times, when reconnection has ceased and the spectra stabilize, as illustrated in Fig. 2, which shows nearly identical spectra from times $t = 3.2$ and $4.3 L_x/c$ for simulations with $B_{gz} = 0$ and $L_z = L_x$ (for three different L_x). For most of our large-system ($L_x = 40\rho_c$) runs, the displayed time of $t = 143/\omega_c = 3.6L_x/c$ is thus sufficiently late to capture final particle distributions.²

Our simulations reach sufficiently large L_x so that the spectral slopes become nearly independent of system size. This is illustrated in Fig. 2, which shows $f(\gamma)$ for runs with $L_x/\rho_c \in \{20, 40, 64\}$, $L_z/L_x = 1$, and $B_{gz} = 0$. While the power law for $L_x/\rho_c = 20$ ($p \approx 2.3$) is slightly steeper than for $L_x/\rho_c = 40$ and 64, the latter two runs have essentially the same $p \approx 2.0$. Similarly, we find for other B_{gz} and L_z that p converges with L_x , within measurement error.

² Magnetic dissipation is essentially finished by $t = 143/\omega_c$ in most cases (Fig. 1, right), except for $B_{gz} = 2$, when the spectra evolved until $t \approx 186/\omega_c = 4.7L_x/c$.

Table 1. Guide field inhibits magnetic energy dissipation and particle acceleration: for each B_{gz} (for both 2D and $L_z = L_x$), we show $\sigma_{h,\text{eff}}$ and the measured change in $U_{\text{mag},xy}$, $U_{\text{mag},z}$, and particle kinetic energy (normalized to initial $U_{\text{mag},xy}$), as well as the particle energy spectral index p (the “error” expresses the fitting uncertainty within a single simulation).

B_{gz}/B_0	$\sigma_{h,\text{eff}}$	L_z/L_x	$\frac{\Delta U_{\text{mag},xy}}{U_{\text{mag},xy}(0)}$	$\frac{\Delta U_{\text{mag},z}}{U_{\text{mag},xy}(0)}$	$\frac{\Delta \text{KE}}{U_{\text{mag},xy}(0)}$	p
0	25	2D	-39%	$\lesssim 0.02\%$	39%	1.9 ± 0.1
0	25	1	-46%	$\lesssim 0.3\%$	46%	2.0 ± 0.1
0.25	9.8	2D	-34%	4%	30%	2.1 ± 0.1
0.25	9.8	1	-36%	5%	31%	2.1 ± 0.1
0.5	3.4	2D	-26%	6%	19%	2.1 ± 0.1
0.5	3.4	1	-26%	5%	20%	2.2 ± 0.1
1	0.96	2D	-15%	4%	11%	3.0 ± 0.5
1	0.96	1	-15%	4%	11%	2.7 ± 0.2
2	0.25	2D	-8%	1%	8%	3.3 ± 0.5
2	0.25	1	-8%	1%	8%	3.3 ± 0.3

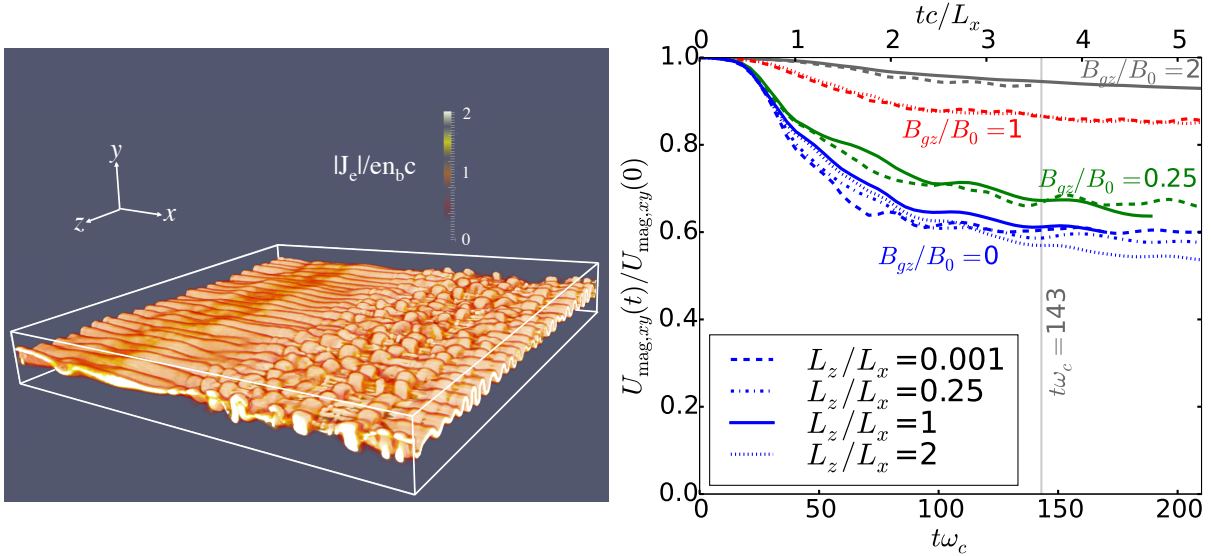


Figure 1. (Left) The electron current density $\|\mathbf{J}\|$ at an early time $t\omega_c = 23$ shows both tearing and kinking of the current layer in a simulation with $L_x = L_z = 64\rho_c$ and $B_{gz} = 0$ (the image shows a narrow range in y around the layer). (Right) Despite the layer kinking, the dissipation of transverse magnetic energy versus time is similar across a range of L_z/L_x , but greatly reduced by increasing B_{gz} .

However, the high-energy cutoff γ_c of the nonthermal power law still increases with system size (Fig. 2). This is expected from our previous cutoff investigation in large 2D systems (Werner et al. 2016) employing a similar, but not identical setup, which showed that, while p converges at modest L_x , similar to the present study, the rise of γ_c with L_x finally saturates only at $L_x/\sigma\rho_0 \sim 200$, well above

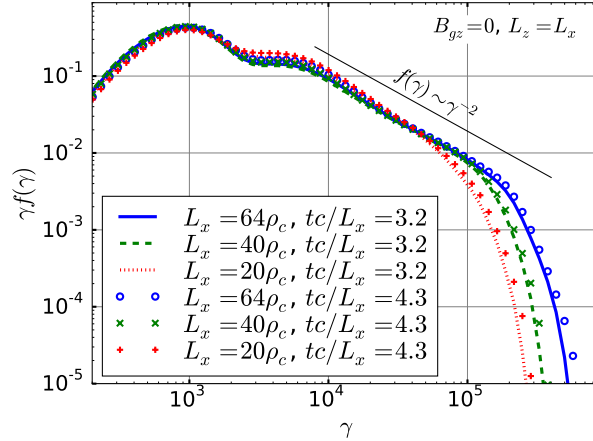


Figure 2. Compensated energy spectra $\gamma f(\gamma)$, for $B_{gz} = 0$ and $L_z = L_x$, saturate at late times; the system size L_x has little effect on the power-law slope, but affects the high-energy cutoff.

the sizes ($L_x/\sigma\rho_0 = 2L_x/\rho_c = 80\text{--}128$) accessible to our present 3D simulations. We thus focus here on p and leave determination of γ_c to future studies. Nevertheless, we note that our simulations achieve cutoff energies (in both 2D and 3D) around $\gamma_c \sim 4\text{--}8\sigma$, comparable (despite the different setup) to the asymptotic, large- L_x cutoff found in (Werner et al. 2016), and to those in our 2D study of relativistic electron-ion reconnection (Werner et al. 2017). This indicates that 3D reconnection can indeed accelerate particles to about the same energies as 2D.

We now characterize the effects of three-dimensionality and guide field on NTPA, comparing simulations with the same size $L_x = 40\rho_c = 80\sigma\rho_0$ but different L_z/L_x and B_{gz} . Our main finding is that, despite fundamental differences in 2D and 3D dynamics (Fig. 1, left), particle acceleration is nearly unchanged by 3D effects, regardless of guide field (Fig. 3). Importantly, 3D relativistic reconnection with weak or no guide field is an efficient particle accelerator, consistent with single simulations run by Sironi & Spitkovsky (2014) and Guo et al. (2014, 2015), but contradicting Zenitani & Hoshino (2007, 2008).³ We see some small differences in p between 2D and 3D in the $B_{gz} = 0$ case (Fig. 3, left); however, for finite guide field, $B_{gz}/B_0 = 0.25$ and 1 (Fig. 3 middle and right), the 2D and 3D spectra are almost identical, probably because strong B_{gz} suppresses dynamical variation in z .

Finally, we find that a sufficiently strong B_{gz} hinders NTPA in 2D and 3D, reducing the number and total energy of accelerated particles, and steepening the power law (see Fig. 4, left). The effects of three-dimensionality and guide field are summarized in Fig. 4 (right), comparing 2D and 3D ($L_z = L_x$) simulations. We conjecture that the lower reconnection rate (hence weaker accelerating electric field) and the smaller available energy budget (Table 1) both contribute to the relative inefficiency and limited range of NTPA for strong guide fields, $B_{gz} \gtrsim B_0$. We further propose that p steepens with B_{gz} because $\sigma_{h,\text{eff}} \sim B_0^2/B_{gz}^2$ decreases [Eq. (2)], and lowering σ_h has been seen to increase p (in $B_{gz} = 0$ 2D studies, Sironi & Spitkovsky 2014; Guo et al. 2014; Werner et al. 2016). Intriguingly, while it does not yield $p \sim 1$ for $\sigma_{h,\text{eff}} \rightarrow \infty$ as those 2D studies suggest, the empirical fit $p \approx 1.9 + 0.7\sigma_{h,\text{eff}}^{-1/2}$, found for $B_{gz} = 0$ semirelativistic electron-ion reconnection (Werner et al. 2017), captures the B_{gz} -dependence found here.

³ Dahlin et al. (2015) nonrelativistic electron-ion reconnection simulations without initial perturbation found more efficient NTPA in 3D due to weaker particle trapping allowing multiple re-acceleration of particles.

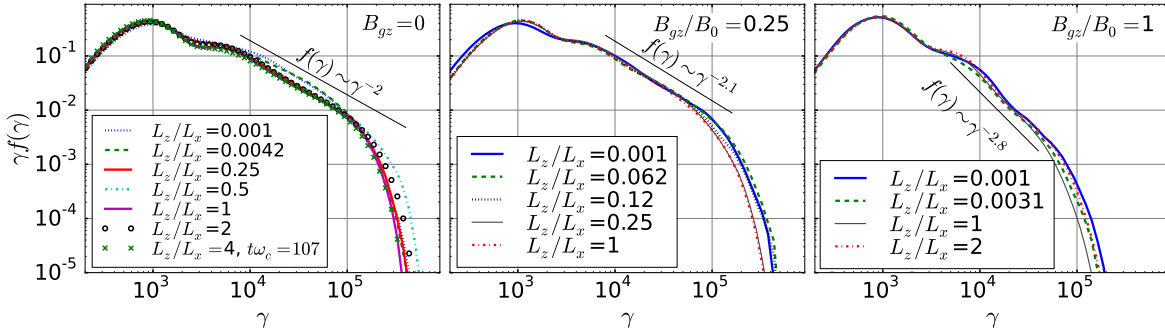


Figure 3. Particle energy spectra for different aspect ratios L_z/L_x , reflecting the importance of 3D effects, for $B_{gz}/B_0 \in \{0, 0.25, 1\}$. The spectra are essentially independent of the aspect ratio. The spectra are shown at $t = 143\omega_c^{-1} = 3.6L_x/c$, except for $L_z/L_x = 4$, $B_{gz} = 0$, shown at $t = 107\omega_c^{-1} = 2.7L_x/c$ when that simulation ended prematurely.

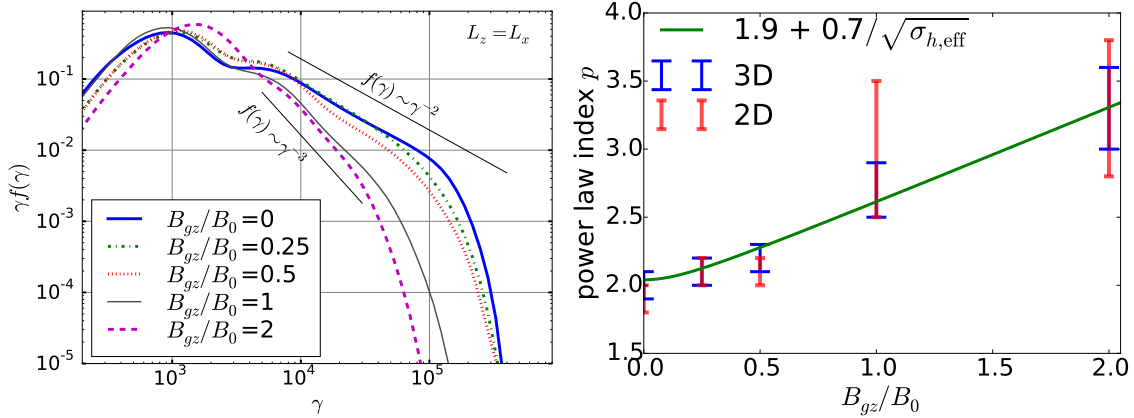


Figure 4. (Left) Strong B_{gz} hinders particle acceleration, as shown by the particle spectra from simulations with $L_z = L_x$ and varying B_{gz} . (Right) The spectral slopes are similar in 2D and 3D, but steepen significantly with strong guide field [Eq. (2)]. The range of p indicates variation within a single simulation.

4. CONCLUSIONS

This Letter presents a systematic first-principles confirmation via PIC simulation that 3D relativistic reconnection in pair plasmas can robustly and efficiently drive nonthermal particle acceleration (NTPA), yielding unambiguous power-law particle distributions despite the presence of RDKI. In addition, the strong influence of guide field on the NTPA power-law index p is described through the dependence of p (see Werner et al. 2017) on the effective hot magnetization $\sigma_{h,\text{eff}}$ including the enthalpy of the guide field. This study thus resolves the long-standing controversy regarding the effects of 3D RDKI structures and guide field on NTPA (Jaroschek et al. 2004; Zenitani & Hoshino 2007, 2008; Sironi & Spitkovsky 2014; Guo et al. 2014). Importantly, our results show that 2D studies are in fact pertinent to 3D reconnection; intriguingly, however, the poorer particle trapping within 3D flux ropes (Dahlin et al. 2015) may allow 3D NTPA to extend beyond the energy cutoff in 2D reconnection (Werner et al. 2016). Our findings lend strong support to reconnection-based models of, e.g., rapid γ -ray flares in the Crab PWN and AGN/blazar jets, prompt GRB emission, and hard-X-ray emission in accreting BH binaries (cf. §1). Furthermore, these results lay the foundation

for characterizing NTPA in realistic 3D reconnection as a function of ambient plasma, helping to diagnose plasma conditions in remote astrophysical systems using observed radiation spectra.

We thank Vladimir Zhdankin and Mitch Begelman for helpful discussions. This work was supported by grants DE-SC0008409, DE-SC0008655 (DOE); NNX12AP17G, NNX16AB28G (NASA); and AST-1411879 (NSF). D.A.U. gratefully acknowledges the hospitality of the Institute for Advanced Study and support from the Ambrose Monell Foundation. Simulations were possible thanks to an INCITE award at the Argonne Leadership Computing Facility, a DOE User Facility supported under Contract DE-AC02-06CH11357. Some 2D simulations were run using XSEDE resources (Townes et al. 2014) supported by NSF grant ACI-1548562, as well as resources provided by the NASA High-End Computing Program through the NASA Advanced Supercomputing Division at Ames Research Center.

REFERENCES

- Arka, I., & Dubus, G. 2013, *A& A*, 550, A101
- Beloborodov, A. M. 2017, arXiv preprint arXiv:1701.02847
- Bessho, N., & Bhattacharjee, A. 2007, *Physics of Plasmas*, 14, 056503
- Bhattacharjee, A., Huang, Y.-M., Yang, H., & Rogers, B. 2009, *Physics of Plasmas*, 16, 112102
- Cerutti, B., Philippov, A., Parfrey, K., & Spitkovsky, A. 2015, *MNRAS*, 448, 606
- Cerutti, B., Uzdensky, D. A., & Begelman, M. C. 2012a, *ApJ*, 746, 148
- Cerutti, B., Werner, G. R., Uzdensky, D. A., & Begelman, M. C. 2012b, *ApJ Lett.*, 754, L33
- . 2013, *ApJ*, 770, 147
- . 2014a, *ApJ*, 782, 104
- . 2014b, *Phys. Plasmas*, 21, 056501
- Coroniti, F. V. 1990, *ApJ*, 349, 538
- Dahlin, J., Drake, J., & Swisdak, M. 2015, *Phys. Plasmas*, 22, 100704
- . 2016, *Phys. Plasmas*, 23, 120704
- Drenkhahn, G., & Spruit, H. C. 2002, *A& A*, 391, 1141
- Giannios, D. 2008, *A& A*, 480, 305
- Giannios, D., Uzdensky, D. A., & Begelman, M. C. 2009, *MNRAS*, 395, L29
- Guo, F., Li, H., Daughton, W., & Liu, Y.-H. 2014, *Phys. Rev. Lett.*, 113, 155005
- Guo, F., Liu, Y.-H., Daughton, W., & Li, H. 2015, *ApJ*, 806, 167
- Jaroschek, C. H., Treumann, R. A., Lesch, H., & Scholer, M. 2004, *Physics of Plasmas*, 11, 1151
- Kagan, D., Milosavljević, M., & Spitkovsky, A. 2013, *ApJ*, 774, 41
- Kirk, J. G., & Skjæraasen, O. 2003, *ApJ*, 591, 366
- Langdon, A. B. 1970, *J. Comput. Phys.*, 6, 247
- Liu, W., Li, H., Yin, L., et al. 2011, *Physics of Plasmas*, 18, 052105
- Liu, Y.-H., Guo, F., Daughton, W., Li, H., & Hesse, M. 2015, *Phys. Rev. Lett.*, 114, 095002
- Loureiro, N., Samtaney, R., Schekochihin, A., & Uzdensky, D. 2012, *Physics of Plasmas*, 19, 042303
- Lyubarsky, Y., & Liverts, M. 2008, *ApJ*, 682, 1436
- Lyubarsky, Y. E. 1996, *A& A*, 311, 172
- Lyutikov, M. 2003, *MNRAS*, 346, 540
- . 2006, *MNRAS*, 367, 1594
- McKinney, J. C., & Uzdensky, D. A. 2012, *MNRAS*, 419, 573
- Melzani, M., Walder, R., Folini, D., Winisdoerffer, C., & Favre, J. M. 2014, *A& A*, 570, A112
- Nalewajko, K., Giannios, D., Begelman, M. C., Uzdensky, D. A., & Sikora, M. 2011, *MNRAS*, 413, 333
- Sironi, L., Giannios, D., & Petropoulou, M. 2016, *MNRAS*, 462, 48
- Sironi, L., Petropoulou, M., & Giannios, D. 2015, *MNRAS*, 450, 183
- Sironi, L., & Spitkovsky, A. 2014, *ApJ Lett.*, 783, L21
- Townes, J., Cockerill, T., Dahan, M., et al. 2014, *Computing in Science & Engineering*, 16, 62
- Uzdensky, D. A. 2011, *Space science reviews*, 160, 45
- Uzdensky, D. A., Cerutti, B., & Begelman, M. C. 2011, *ApJ Lett.*, 737, L40
- Uzdensky, D. A., Kulsrud, R. M., & Yamada, M. 1996, *Phys. Plasmas*, 3, 1220

- Uzdensky, D. A., Loureiro, N. F., & Schekochihin, A. A. 2010, *Phys. Rev. Lett.*, 105, 235002
- Uzdensky, D. A., & Spitkovsky, A. 2014, *ApJ*, 780, 3
- Werner, G. R., Uzdensky, D. A., Begelman, M. C., Cerutti, B., & Nalewajko, K. 2017, submitted, arXiv:1612.04493
- Werner, G. R., Uzdensky, D. A., Cerutti, B., Nalewajko, K., & Begelman, M. C. 2016, *ApJ Lett.*, 816, L8
- Zenitani, S., & Hoshino, M. 2001, *ApJ Lett.*, 562, L63
- . 2005, *ApJ Lett.*, 618, L111
- . 2007, *ApJ*, 670, 702
- . 2008, *ApJ*, 677, 530